Controling the single-diamond nitrogen-vacancy color center photoluminescence spectrum with a Fabry-Perot microcavity

Yannick Dumeige, Romain Alleaume, Philippe Grangier, François Treussart, Jean-François Roch

To cite this version:

Yannick Dumeige, Romain Alleaume, Philippe Grangier, François Treussart, Jean-François Roch. Controling the single-diamond nitrogen-vacancy color center photoluminescence spectrum with a Fabry-Perot microcavity. New Journal of Physics, 2011, 13, pp.025015. 10.1088/1367-2630/13/2/025015 . hal-00578573

HAL Id: hal-00578573
https://hal.science/hal-00578573v1

Controling the single-diamond nitrogen-vacancy color center photoluminescence spectrum with a Fabry–Perot microcavity

2011 New J. Phys. 13 025015

(http://iopscience.iop.org/1367-2630/13/2/025015)

New Journal of Physics
The open-access journal for physics

Controling the single-diamond nitrogen-vacancy color center photoluminescence spectrum with a Fabry–Perot microcavity

Yannick Dumeige[1,5], Romain Alléaume[2], Philippe Grangier[3], François Treussart[4] and Jean-François Roch[4]

[1] Université Européenne de Bretagne, Laboratoire Foton,
CNRS UMR 6082 Foton, Enssat, 6 rue de Kerampont,
22305 Lannion Cedex, France
[2] Institut Télécom/Télécom ParisTech, Laboratoire Traitement et
Communication de l'Information, CNRS UMR 5141, 46 rue Barrault,
75634 Paris Cedex, France
[3] Laboratoire Charles Fabry de l'Institut d'Optique, CNRS UMR 8501,
Institut d'Optique Graduate School, Campus Polytechnique—RD 128,
2 avenue Augustin Fresnel 91127 Palaiseau Cedex, France
[4] Laboratoire de Photonique Quantique et Moléculaire, CNRS UMR 8537,
École Normale Supérieure de Cachan, 61 avenue du Président Wilson,
94235 Cachan Cedex, France
E-mail: yannick.dumeige@univ-rennes1.fr

New Journal of Physics **13** (2011) 025015 (21pp)
Received 20 September 2010
Published 21 February 2011
Online at http://www.njp.org/
doi:10.1088/1367-2630/13/2/025015

Abstract. We present here both theoretical and experimental results on the fluorescence of single defect centers in diamond nanocrystals embedded in a planar dielectric microcavity. From a theoretical point of view, we show that the overall fluorescence collection efficiency using a moderate numerical aperture microscope objective can be enhanced by using a low-quality-factor microcavity. This could be used in particular for low-temperature applications, where the numerical aperture of collection microscope objectives is limited due to the experimental constraints. We experimentally investigate the control of the fluorescence spectrum of the emitted light from a single center. We show the simultaneous narrowing of the room temperature broadband emission spectrum and the increase in the fluorescence spectral density.

---

[5] Author to whom any correspondence should be addressed.

1367-2630/11/025015+21$33.00

Contents

1. Introduction

Single nitrogen-vacancy (NV) defect centers in diamond are a promising candidate for solid-state quantum computing and quantum information processing (QIP) applications [1]. It has been shown that the NV center can be used as a reliable source of single photons [2] for quantum key distribution (QKD) [3, 4] and single-photon interferences [5]. More recently, its potentialities as a spin qubit with a very long spin coherence time [6] have been successfully demonstrated in the context of coherent coupling of NV^- electronic spin to single neighboring nuclear spins [7, 8]. It takes advantage of both the spin coupling to optical transitions and the optical readout of the associated electron spin resonance [9], which recently led to the realization of quantum entanglement between the polarization of a single optical photon and the solid-state qubit associated with the NV^- single electronic spin [10]. The spin and optical properties of a single NV center were also used to probe magnetic fields at the nanoscale [11, 12].

In both QIP and QKD applications, efficiency in the collection of radiated photons is crucial. The rate of qubit exchange in QKD or the efficiency of optical readout in QIP strongly depends on the external quantum yield. To control their spontaneous emission rate or to increase their fluorescence collection, solid-state individual emitters can be embedded in an optical microcavity [13, 14]. For NV center systems, different configurations of coupling with a microcavity have been investigated. Some efforts have been made in designing diamond photonic crystal microcavities [15]–[17]. Microcavities with a quality factor Q of around 600 have been fabricated in a thin photonic crystals membrane [18]. Due to the difficulty of obtaining monolithic microcavities from bulk or nanocrystalline diamond [19], other approaches based on hybrid structures have been used. Normal mode splitting has been observed in a system consisting of diamond nanocrystals coupled to the whispering gallery mode (WGM) of a silica microsphere [20]. The coupling of a single NV center to a high-Q WGM resonator has been observed in silica microdisks [21] or microspheres [22, 23]. By using a fiber taper, a single diamond nanocrystal has been positioned onto a silica WGM toroid, which demonstrates the possibility of manipulating non-classical emitters to couple them with high-Q microresonators [24]. GaP WGM microdisks have also been used to efficiently collect at the chip scale the fluorescence of NV centers [25]. To reach a very low mode volume, an optimization scheme of the TiO_2/SiO_2 micropillar Bragg cavity has been proposed [26]. Alternatively, a hybrid structure involving photonic crystals in silicon nitride [27] or GaP [28] enabling coupling to NV centers has been proposed for reaching high Q. In this context, the controlled coupling of a single diamond nanocrystal to planar Si_3N_4 or GaP photonic crystal heterostructures [29]–[31] and the emission spectrum modification of a single NV center embedded in an opal photonic crystal structure made of polystyrene microspheres [32] were experimentally demonstrated. Finally, one-dimensional photonic nanostructures consisting of diamond nanowires can also be used to enhance the single-photon emission from NV centers [33].

In most of the previous cases, the goal was to obtain simultaneously a high Q and a small mode volume in order to enhance the Purcell factor [34] and reach the regime in which the emitter spontaneous emission rate is strongly affected by its coupling to a cavity mode. This results in enhanced spectral properties of the single-photon source well adapted to GHz repetition rate QKD [35].

However, not only can the emission rate be strongly modified but also the radiation pattern of the emitter [36, 37]. The modification of the fluorescence spectrum of broadband emitters by photonic structures has also been thoroughly investigated. In this last case, the dispersion associated with its dielectric environment leads to a renormalization of the emitter spectrum, which is such that a simple planar microcavity can strongly modify the emission spectrum of an organic dye [38]–[41] or of a colloidal CdSe/ZnS nanocrystal [42] without loss of total intensity, as shown in the pioneering work [43].

In this work, we show that the use of a planar microcavity can lead to an increase in the radiated power per nanometer bandwidth. This could help in practical configuration of QIP or QKD: (i) at low temperature, a microcavity resonant with the zero-phonon line (ZPL) could enhance this transition at the expense of the ones associated with the phonon sidebands [30] with expected improvements in entanglement schemes [10]; (ii) many experiments would be better performed with monochromatic single-photon sources; for instance, the first single NV source QKD demonstration had required the use of broadband electro-optical modulators [3]. With a cavity, the broad phonon sideband can be squeezed into a narrow band without loss of intensity. We also demonstrate that the microcavity can be used to tune the emission spectrum. This paper consists of two theoretical and experimental parts. The first part begins with a description of the planar microcavity structure. We then present the calculation method used to determine the fluorescence power collected by the microscope objective from a single NV color center located either on top of a high-reflectivity (HR) mirror or inside the microcavity. We consider both the cases of the monochromatic emission (standing for cryogenic operation of the NV center emission) and the room-temperature broadband emission. In the second part, we describe the experimental setup and the observations showing modifications of the emission associated with the coupling of a single NV color center in a nanodiamond to a single longitudinal mode of the planar dielectric microcavity.

2. Calculation of the total fluorescence power P_{tot} collected from a single emitting dipole coupled to a planar Fabry–Perot microcavity

The collection of light from a single emitter embedded in a dielectric material with a high index of refraction, such as the NV color center in bulk diamond or semiconductor quantum dots, has similar issues to those of semiconductor light emitting diodes (LED). They mainly come from the light trapping due to total internal reflections. Many theoretical and experimental studies have shown that the light collection efficiency of LED can be enhanced by using a planar microcavity [44, 45]. This concept has been adapted to high index of refraction solid-state single-photon sources [14].

In the case of the NV color center in diamond nanocrystals, it has been pointed out that refraction is irrelevant due to the small dimensions of the nanocrystals compared to the emission wavelength and that the emitter can be assumed as a point source emitting in the surrounding dielectric medium [46]. This feature enhances the collection efficiency.

In this section, we will show that the use of a resonant microcavity combined with the nanocrystal approach can also increase the collection efficiency for NV defect centers. By using an HR rear mirror, the isotropic radiation is redirected in the same half-space [47], while the microcavity simultaneously narrows the emission spectrum [48], both effects resulting in a larger spectral density of the collected light intensity. Finally, for an appropriate choice of the emitting dipole position and orientation, one can also benefit from the local electromagnetic field enhancement [44].

2.1. Microcavity—single emitter structure

The single-photon source described in figure 1 consists of a nanocrystal embedded in a thin polymer layer deposited on a dielectric HR Bragg mirror made of 16 periods of two materials of high n_{h} and low n_{ℓ} indices of refraction [49].

The cavity is obtained using a second low-reflectivity (LR) mirror made of $N < 16$ periods of the same materials. The resonant wavelength of the microcavity can be tuned by changing the air gap d_0 between the LR Bragg mirror and the HR mirror. The thicknesses of the different layers of the Bragg mirrors have been chosen to obtain a central wavelength λ_0 around $\lambda_{\mathrm{NV}}^{\mathrm{max}} = 680\,\mathrm{nm}$, corresponding to the peak emission of the NV$^-$ center at room temperature. The structure has also been optimized to maximize the electric field amplitude in the polymer layer containing the nanocrystals. We present in figure 1 the electric field amplitude distribution for a normal incidence plane wave in the two cases we extensively study in this paper: (a) an HR mirror without a second mirror and (b) a microcavity with $N = 4$.

Figure 2 presents the dispersion relation $\omega(k_{\parallel})$ of the Bragg mirrors, where ω is the angular frequency and $k_{\parallel}$ is the in-plane component of the wavevector $\mathbf{k}$ [50]. Due to the field penetration in the dielectric mirror, the minimal interference order for the planar microcavity is given by $m_{\mathrm{c}} = \lfloor \overline{n}/\Delta n \rfloor + 1$ with $\Delta n = n_{\mathrm{h}} - n_{\ell}$, $\overline{n} = n_{\mathrm{h}} n_{\ell}/n_{\mathrm{a}}$ and $n_{\mathrm{a}} = (n_{\ell} l_1 + n_{\mathrm{h}} h_1)/(l_1 + h_1)$, where $\lfloor x \rfloor$ is the floor function of x [44]. With our refractive index values, we obtain $m_{\mathrm{c}} = 3$, which is used to obtain the microcavity dispersion curves displayed in figure 2 as solid lines.

The dispersion relation is obtained noting first that $k = \sqrt{k_{\parallel}^2 + k_z^2}$. Then, if we call L_{cav} and n_{cav} the effective length and refractive index of the cavity, taking into account the

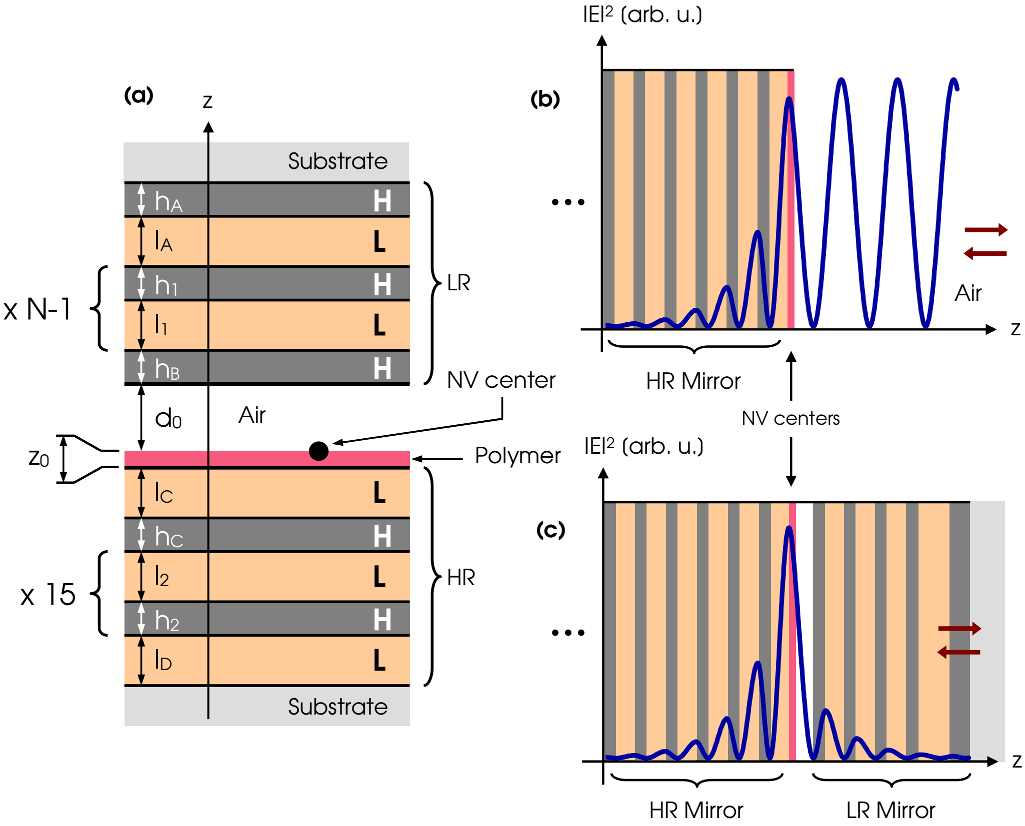

Figure 1. (a) Scheme of the single-photon source microcavity consisting of a diamond nanocrystal containing a single NV center, positioned in the air gap between the two mirrors of a planar Fabry–Perot microcavity. The lower HR Bragg mirror is composed of a fixed number of 16 periods, whereas the upper LR mirror is made of N periods. Referring to the figure annotations, the thickness values of the different layers are $h_A = 134$ nm, $l_A = 171.7$ nm, $h_1 = h_2 = h_B = 73.1$ nm, $l_1 = l_2 = 113.7$ nm, $h_C = 75.3$ nm, $l_C = 110.1$ nm and $l_D = 117.1$ nm. The single NV color center is assumed to be located on the top of the polymer layer of thickness $z_0 = 25$ nm. d_0 is the adjustable air gap thickness. The low index of refraction ($n_\ell = 1.4745$ at $\lambda = 680$ nm) SiO_2 layers are marked ‘L’ and the high index ($n_h = 2.2925$) Nb_2O_5 layers are marked ‘H’. The refractive indices of the polymer and of the fused silica substrate are, respectively, $n_p = 1.49$ and $n_s = 1.4556$. We also give the optical intensity distribution $|E(z)|^2$ at λ_{NV}^{max} for a plane wave excitation in normal incidence. The calculations have been performed using the transfer-matrix method [50] for (a) the HR mirror and (b) the microcavity with $\lambda_0 = \lambda_{NV}^{max}$ and $N = 4$.

penetration depth in the Bragg mirrors, we obtain $2k_z L_{cav} = 2m_c\pi$ for a resonant mode and thus

$$\omega = \frac{c}{n_{cav}}\sqrt{k_\parallel^2 + \left(\frac{m_c\pi}{L_{cav}}\right)^2}. \tag{1}$$

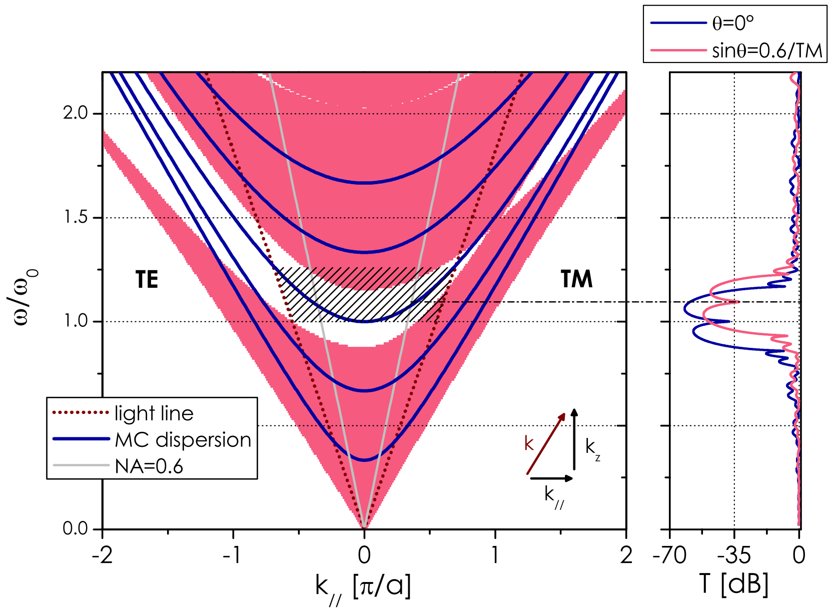

Figure 2. Graphical representation of the Bragg mirror and microcavity dispersion relations (left) and of the transmission spectrum (right). The TE (resp. TM) polarization case is displayed on the negative (resp. positive) $k_\parallel$ side. $a = l_1 + h_1$ is the period of the Bragg mirror. The propagation is forbidden in the white areas and allowed in the pink areas. The planar microcavity (MC) dispersion curves are also represented (in blue), assuming an interference order $m_c = 3$ for λ_0 in normal incidence. We have added two light lines: the one associated with a full half-space collection (numerical aperture (NA) = 1, red dot line) and the other for a restricted collection of light with NA = 0.6 optics (gray line). Right graph: the transmission spectrum $T(\omega, \theta, \mathrm{TM})$ of the microcavity ($N = 4$ case) in dB units either at normal incidence ($\theta = 0°$, blue curve) or in the case of inclined incidence with $\sin\theta = 0.6$ and TM polarization (red curve). These curves display dips at their resonant wavelengths. The dashed region on the left graph indicates the range of frequencies allowed in the case of NA = 1. Note that for NA = 0.6, only frequencies shorter than the resonance frequency are allowed, which explains why the experimental spectra displayed in figures 8 and 9 are asymmetric, with a steep falling edge on the high frequency side.

Neglecting the polymer layer effect, the two quantities L_{cav} and n_{cav} can be estimated by solving the resonance equation (for $d_0 \approx 135$ nm),

$$m_c \frac{\lambda_0}{2} = 1 \times d_0 + n_a (L_{\mathrm{cav}} - d_0) = n_{\mathrm{cav}} L_{\mathrm{cav}}. \tag{2}$$

We note that with the microcavity design, the dispersion curve referring to $m_c = 3$ is fully included in the first forbidden band of the Bragg mirror for both TE and TM polarizations and for the maximal numerical aperture considered here (i.e. NA = 1, corresponding to the light line) and thus also for the value NA = 0.6 used in the experiments. This feature is important for room temperature experiments, since in this case the fluorescence spectrum of NV centers is broad (full-width at half-maximum (FWHM) ≈ 75 nm) and therefore requires a broadband

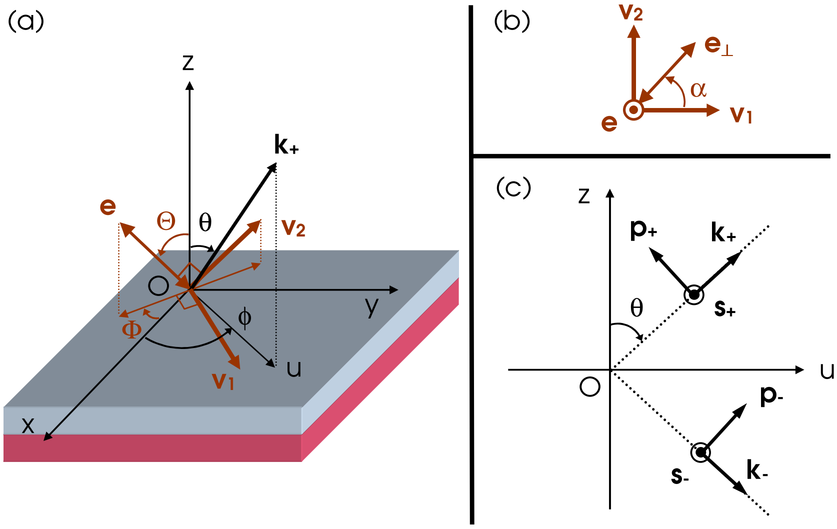

Figure 3. (a) O is the position of the orthogonal ($\mathbf{e}$, $\mathbf{e}_\perp$) dipoles that we associate with the NV$^-$ color center transition. The orientation of the component $\mathbf{e}$ is described by two angles (Θ, Φ) relative to the Bragg mirrors plane (x, y). $\mathbf{k}_+$ is the wavevector of the field in the upper half-space emitted in the direction (θ, ϕ). (b) α refers to the orientation of $\mathbf{e}_\perp$ in the plane ($\mathbf{v}_1$, $\mathbf{v}_2$) orthogonal to $\mathbf{e}$. (c) $\mathbf{k}_-$ is the wavevector of the field emitted in the same direction but in the lower half-space. The unitary vectors are denoted $\mathbf{s}_\pm$ (resp. $\mathbf{p}_\pm$) for TE (resp. TM) polarization.

operation range. We also show the transmission spectrum $T(\omega, \theta, \mathrm{TM})$ obtained using the standard transfer matrix method [50] for a microcavity with $N = 4$ both for the normal incidence and for the $\sin\theta = 0.6$ TM polarization cases. Note that due to the unbalanced mirror reflectivity, the resonant transmission is weak even though we assumed lossless materials.

This simple linear analysis [14] allows two properties of the microcavity to be revealed: (i) for the value NA=0.6 used in our experiment, it is possible to efficiently collect light coupled to the resonant mode of the cavity; (ii) in the case of a broadband emission, the blue-shift of the cavity resonance explains the spectrum asymmetry experimentally observed (see section 3).

2.2. Calculation method of the total collected power P_{tot} radiated by a single nitrogen-vacancy (NV) color center inside the microcavity

It has been well established since the early studies of the NV$^-$ color center [51] that it has two orthogonal incoherent electric dipole transitions oriented in the plane perpendicular to the [111] crystallographic direction (along the N-V axis), as exemplified in the context of recent studies on polarization selective excitation of this color center [52, 53].

In the following, we will model the NV$^-$ center by two identical orthogonal dipoles ($\mathbf{e}$, $\mathbf{e}_\perp$). The dipoles are assumed to be located in O. $\mathbf{e}$ orientation is defined by two angles Θ and Φ relative to the Bragg mirror plane (x, y), such as $\mathbf{e} = (\sin\Theta\cos\Phi, \sin\Theta\sin\Phi, \cos\Theta)$ in the sample plane coordinate system, as represented in figure 3. Thus the second dipole can be written $\mathbf{e}_\perp = \mathbf{v}_1\cos\alpha + \mathbf{v}_2\sin\alpha$ with $\mathbf{v}_1 = (-\sin\Phi, \cos\Phi, 0)$ and $\mathbf{v}_2 = (-\cos\Theta\cos\Phi,$

$-\cos\Theta\sin\Phi, \sin\Theta)$. The most favorable configuration for efficiently collecting the photoluminescence of the NV$^-$ color center corresponds to $(\Theta = \pi/2, \alpha = 0)$, whereas the worst configuration is obtained for $\Theta = 0$. In the experiment, we selected the brightest emitters, which are the ones having the strongest in-sample plane dipole components. Therefore, in the following, we restrict our calculation of the collected power P_{tot} to this configuration $(\Theta = \pi/2, \alpha = 0)$. To calculate the power radiated by the two dipoles in the upper half-space $(z > 0)$, we used the transfer-matrix method of [54].

For a given direction of radiation characterized by the wavevector $\mathbf{k}_+$, with the coordinate $\mathbf{k}_+ = k(\sin\theta\cos\phi, \sin\theta\sin\phi, \cos\theta)$, the wave can be either TE-polarized along $\mathbf{s}_+$ or TM-polarized along $\mathbf{p}_+$. $\mathbf{s}_+$ is the unit vector orthogonal to the incidence plane (u, z), whereas $\mathbf{p}_+$ is calculated by

$$\mathbf{p}_+ = \frac{1}{k}\mathbf{s}_+ \times \mathbf{k}_+. \tag{3}$$

The wavevector of the field related to $\mathbf{k}_+$ propagating in the opposite direction is denoted $\mathbf{k}_- = k(\sin\theta\cos\phi, \sin\theta\sin\phi, -\cos\theta)$. We also have $\mathbf{s}_- = \mathbf{s}_+$ and the same relation as equation (3) holds for $\mathbf{p}_-$. According to the method given in [54] and using the dipole description of [37] and [55], the source terms for the two propagation directions are

$$A_+^s = \mathbf{e}\cdot\mathbf{s}_+, \quad A_+^p = \mathbf{e}\cdot\mathbf{p}_+, \quad A_-^s = -\mathbf{e}\cdot\mathbf{s}_- \text{ and } A_-^p = \mathbf{e}\cdot\mathbf{p}_-. \tag{4}$$

We have the same relations for $\mathbf{e}_\perp$. Using these expressions for the optical sources, it is possible to calculate the spectral density of the radiated power per solid angle $\mathrm{d}^3P/(\mathrm{d}\Omega\,\mathrm{d}\lambda)$ for a given $\mathbf{k}_+$ by summing the power emitted by the two incoherent dipoles [54]. Following the method described in [40], the full radiated power collected by the air microscope objective of $\mathrm{NA} = \sin\theta_{\mathrm{M}}$ in a spectral window of full-width $\Delta\lambda$ is then evaluated by

$$P_{\mathrm{tot}} = \int_{\lambda_0-\Delta\lambda/2}^{\lambda_0+\Delta\lambda/2} f(\lambda)\,\mathrm{d}\lambda \int_0^{2\pi}\mathrm{d}\phi \int_0^{\theta_{\mathrm{M}}} \frac{\mathrm{d}^3P}{\mathrm{d}\Omega\,\mathrm{d}\lambda}\sin\theta\,\mathrm{d}\theta, \tag{5}$$

where $f(\lambda)$ is the free space emission normalized spectrum function, which will be assumed for simplicity to have a Gaussian profile centered at $\lambda_{\mathrm{NV}}^{\mathrm{max}}$ with an FWHM B.

2.3. *Calculation of P_{tot}*

Our aim is to show that the light extraction from a single emitter can be increased using a low-finesse microcavity in practical cases. Consequently, we will take as the reference the case of dipoles located on a single mirror. The advantage of this last configuration with respect to free space is twofold: the mirror redirects the fluorescence in the same half-space and if the dipoles are located in a field antinode, their emission rate is increased [44, 47]. In the following, we consider two cases: (1) the monochromatic emission of NV$^-$ at its ZPL wavelength $\lambda_{\mathrm{ZPL}} = 637$ nm, which corresponds to cryogenic operation; (2) the broadband emission case, associated with room temperature photoluminescence.

2.3.1. Monochromatic case. First we focus on the low temperature configuration. In this particular case, the fluorescence spectrum of the emitter is assumed to be quasi-monochromatic and the ZPL has a bandwidth around $B = 0.3$ nm [56, 57]. For simplicity and because our cavity has been optimized for a resonant wavelength of 680 nm, we have used for the calculation $\lambda_{\mathrm{NV}}^{\mathrm{max}}$ as the emission wavelength instead of λ_{ZPL}.

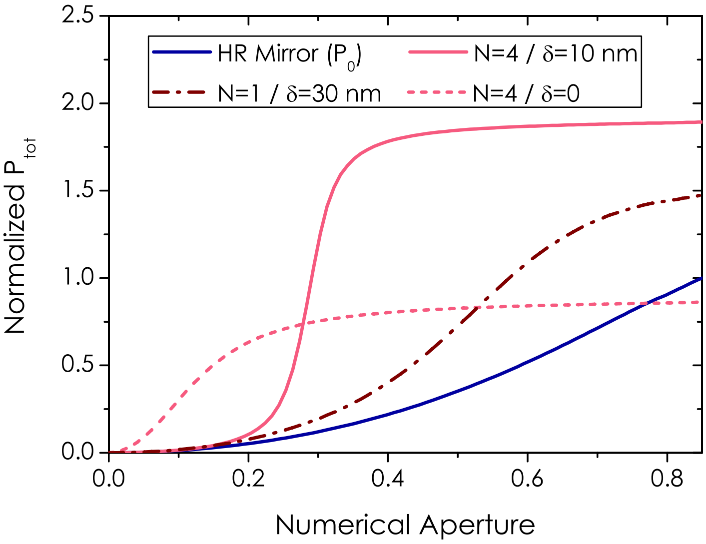

Figure 4. Full radiated power P_{tot} in the case of a narrow bandwidth emitter (single NV$^-$ color center emitting at $\lambda_{\mathrm{NV}}^{\max}$) as a function of the numerical aperture of the collection objective. The calculations have been performed for a single HR mirror and in the case of the microcavity for two values of N and different values of the microcavity mode—emitter wavelength detuning δ. The results are normalized to the value of P_{tot} corresponding to the HR mirror case and at the maximal numerical aperture collection (NA = 0.85).

To collect the light across the fused silica substrate of the LR mirror in the case of the microcavity configuration, we use a long working distance objective with NA = 0.6. The reference configuration consists of an HR mirror and a microscope objective with NA = 0.85. We used this low value of NA because it is suited to the cryogenic setup [56]. The simulation results are shown in figure 4. In the case of a low-finesse cavity ($N = 1$) and a detuning $\delta = \lambda_0 - \lambda_{\mathrm{NV}}^{\max} = 30\,\mathrm{nm}$, we observe an increase of about 50% in the collection efficiency with respect to the reference case. This can be increased by using a better finesse ($\mathcal{F} \approx 60$) cavity ($N = 4$). Note that in this case, the cavity must be slightly positively detuned ($\delta = 10\,\mathrm{nm}$) to obtain the maximal collection increase of about 80%. This positive detuning allows the spectral overlap between the emission spectrum and the microcavity dispersion to be optimized, as illustrated by the hatched area in figure 2. For $\delta = 0$, we do not observe any increase in the extracted fluorescence for the maximal numerical aperture.

2.3.2. Broadband emission. At room temperature, the coupling between the radiative transitions of the NV$^-$ color center and the diamond matrix phonon broadens the emission spectrum, yielding an FWHM linewidth of about $B = 75\,\mathrm{nm}$ due to the phonon replica.

Figure 5(a) gives the calculation of the full radiated power with no additional filter, whereas figure 5(b) presents the same calculations with a $\Delta\lambda = 40\,\mathrm{nm}$ band-pass filter whose resonant wavelength is chosen in order to increase the overall radiated power for the maximal numerical aperture. This filter could be useful, for example, in open space QKD applications where it will reject a large amount of background light [4]. As was the case for monochromatic emission, the enhancement is better for $N = 4$ and for a positive detuning. The maximal enhancement is

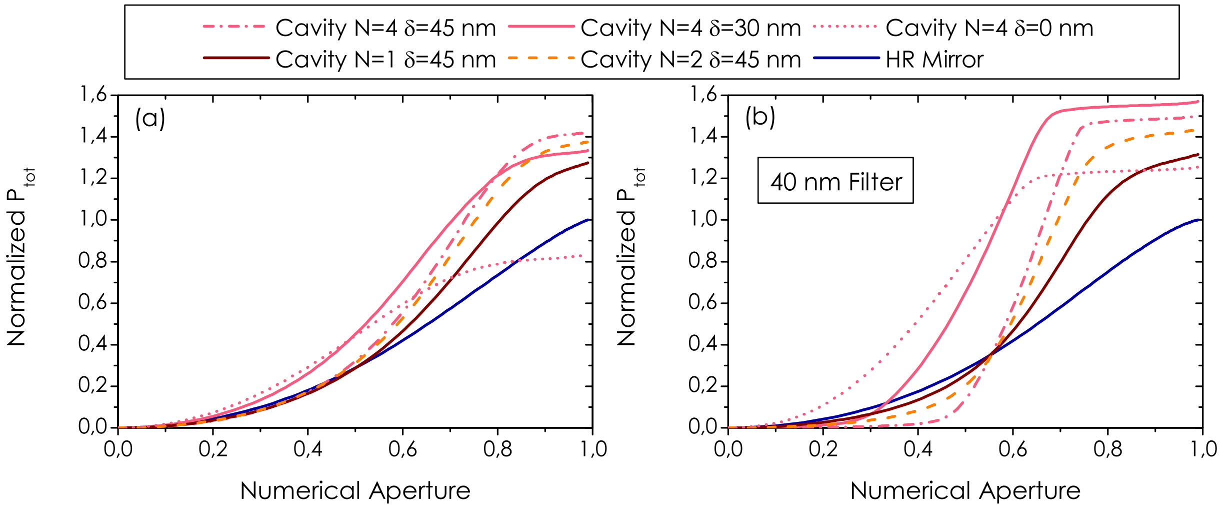

Figure 5. Full radiated power P_{tot} in the case of a broadband emitter as a function of the numerical aperture of the collection objective (a) without additional filter and (b) with a $\Delta\lambda = 40\,\mathrm{nm}$ band-pass filter. The calculations have been performed for a single HR mirror and for microcavities with three values of N and different values of the microcavity mode—emitter wavelength detuning δ. The results are normalized to the value corresponding to the HR mirror and the maximal numerical aperture (NA = 1).

weaker than in the previous configuration, since in room temperature experiments it is possible to use larger numerical aperture collection objectives with NA close to unity. Note that the collection efficiency enhancement is improved by the band-pass filter, as shown in figure 5(b). This effect comes from the increase in the coherence length due to the coupling of emitted light to the microcavity mode, similarly to what has already been observed in microcavity LED [58]. We can underline furthermore this phenomenon by calculating the enhancement ratio P_{tot}/P_0, where P_0 is the radiated power by the HR mirror at the same NA as the one used to calculate P_{tot}. The corresponding results are shown in figure 6(a) for the full spectrum and in figure(b) for the filtered spectrum. We note that the maximal collection efficiency is reached for NA > 0.6. For NA = 0.6 and $\delta = 30\,\mathrm{nm}$, detuning the maximal enhancement is increased by 1.7 for the full bandwidth detection (figure 6(a)) and by 2.75 for the filtered detection (figure 6(b)).

At low NA < 0.6 and filtered detection, the collected power is reduced in the microcavity case ($N = 4$) with respect to the mirror case for detuning larger than $\delta = 30\,\mathrm{nm}$. This situation is reversed if one uses smaller detuning values, as can be seen for $\delta = 30\,\mathrm{nm}$ and $\delta = 0$ in figure 6(b). Indeed, for low numerical apertures, a large positive detuning has a detrimental role since the cavity resonance would be obtained for too large angles of incidence, out of the collection aperture.

Finally, we have also calculated that for NA < 0.82 and the configuration $N = 4$, $\delta = 30\,\mathrm{nm}$, the total collected power in the case of the filtered detection is larger than the full bandwidth detection one with only the HR mirror.

Note that the evolution of P_{tot} versus NA obtained for the optimal NV color center dipoles orientation holds for all possible orientations. For broadband emission, in the worst configuration $\Theta = 0$ and in the case of NA = 0.6, the same P_{tot} calculation methods yield a total

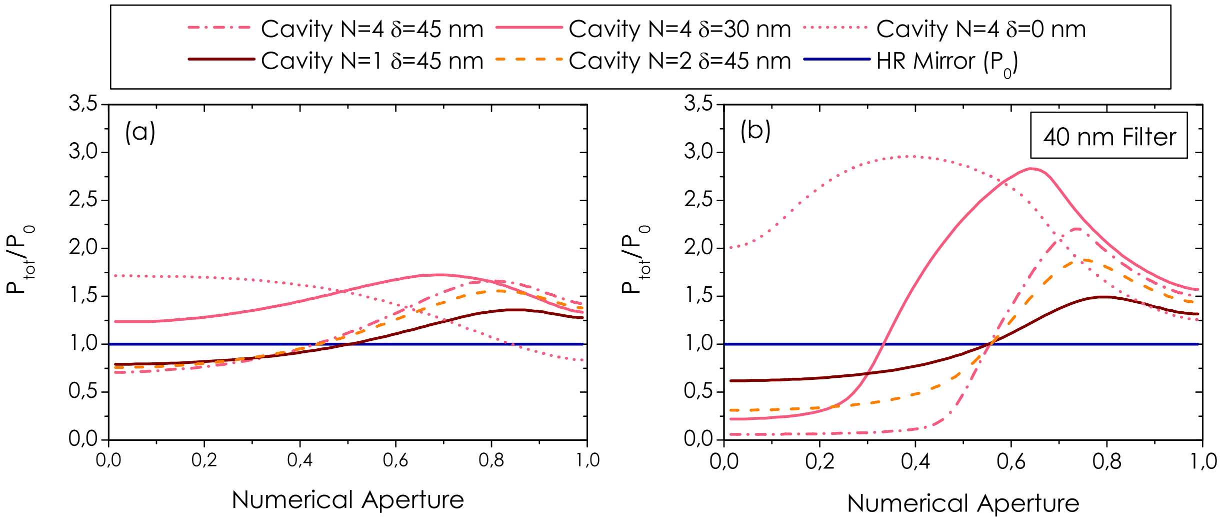

Figure 6. Enhancement factor of the total collected power P_{tot} versus the NA in the case of the microcavity with respect to the HR mirror configuration, for which the collected power is P_0 (a) without additional filter and (b) with a $\Delta\lambda = 40$ nm band-pass filter. The power P_{tot} is calculated in the same way as in figure 5.

collected power equal to 53% of the one of the best configuration in the case of the HR Bragg mirror. Similar results are obtained in the case of an $N = 4$ microcavity, for which the total collected power in the worst dipole orientation case corresponds to 50% of total power in the optimal case.

As a conclusion, the simulation shows that the collection of photoluminescence from a single NV^- color center can be increased by its coupling to one low–order mode of a planar microcavity. Even in the case of broadband emission, the use of a moderate finesse ($\mathcal{F} \approx 60$) can enhance the collection efficiency. In addition, such coupling also leads to a narrowing of the emitted spectrum and thus to an increase in the coherence length of the emitted light.

3. Experimental measurement of the spectral properties of the NV color center coupled to a single mode of the planar microcavity

3.1. Experimental setup

The single emitter studied in this work is an NV^- color center in type 1b (natural specified content in nitrogen ≈200 ppm) diamond nanocrystals (Micron + MDA 0–0.1 from De Beers/Element6) with a size smaller than 100 nm, obtained by a high-pressure and high-temperature synthesis. To increase the natural content of the NV center in the nanodiamonds, the particles were irradiated by a high-energy electron beam to generate vacancies and then annealed during 2 h at 800 °C under vacuum. Then, they were cleaned by oxidative chemicals and dispersed in a propanol solution containing a polymer at low concentration (polyvinylpyrrolidone, 1% w/w). The mean hydrodynamical size of the nanodiamond in the colloidal suspension is 90 nm, as measured by dynamic light scattering. The nanodiamond–polymer solution is finally spin-coated onto the HR dielectric mirror, forming a 25 nm-thick polymer layer with a surface concentration of about one nanocrystal per 10 μm^2.

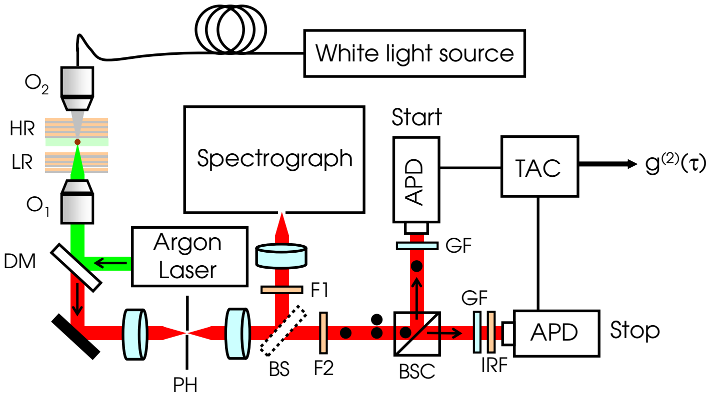

Figure 7. Scheme of the setup used to study the fluorescence from a single NV color center in diamond. O$_1$, microscope objective (long working distance, $\times 40$; NA $= 0.60$); O$_2$, microscope objective ($\times 16$; NA $= 0.32$); PH, pinhole of 50 μm diameter; BS, beam-splitter plate; F1, glass filter (Schott OG550) transmitting $\lambda > 550$ nm; F2, interference filter transmitting $\lambda > 580$ nm and removing the remaining light at the pump wavelength; BSC, non-polarizing 50/50 beam-splitter cube; APDs, silicon avalanche photodiodes in the photon counting regime; IRF, interference filter suppressing near-infrared light at $\lambda > 740$ nm, which is combined with two glass filters (GF; Schott KG4), resulting in suppression of the optical crosstalk between the APDs due to their breakdown flash [59]. TAC, Time to Amplitude Converter connected to a multichannel analyzer board, allowing us to extract the time intensity second-order correlation function $g^{(2)}$.

The microcavity is obtained by placing an LR mirror ($N = 4$ reflectivity, $R_{\mathrm{LR}} \approx 90\%$) in front of the HR mirror (reflectivity $R_{\mathrm{HR}} \approx 99.99\%$) at a distance that can be adjusted using micrometric screws and piezoelectric actuators. From an experimental point of view, the actual values of layer thicknesses for the HR mirror are $h_2 = 75.3$ nm and $l_2 = 117.1$ nm.

Figure 7 is a schematic diagram of the confocal optical scanning microscope [60] used to study the fluorescence of a single NV center in a dielectric microcavity. The light at 514.5 nm wavelength from a cw argon-ion laser is focused on the nanodiamond-polymer layer through the LR mirror, with a long working distance microscope objective O$_1$ having NA $= 0.6$. The objective O$_1$ can be corrected to cross the 1 mm thick fused silica substrate of the LR mirror, thanks to a correction collar. This collar can also be set to a position allowing use of the objective right in front of the HR mirror without the additional LR mirror. The LR mirror has a reflectivity of less than 20% in the range of 500–550 nm, allowing for efficient excitation at the laser wavelength. The sample is raster scanned with a piezoelectric stage. The fluorescence from NV centers is collected through the same objective O$_1$, the detection volume being defined by a confocal pinhole. The collected light passes through a dichroic mirror and long-pass filters are used to remove any residual excitation light. The fluorescence light intensity is equally divided into a first beam for spectral analysis by an imaging spectrograph (composed of a grating and a cooled CCD array for spectrum record) and a second beam for measuring the photon statistics using the standard Hanbury–Brown and Twiss (HBT) coincidence setup. The latter measurement allows us to identify the emission of a single-color center yielding a perfect photon antibunching. The white light source and the microscope objective O$_2$ are used to measure the microcavity transmission spectrum. Note that in our experimental configuration we obtain

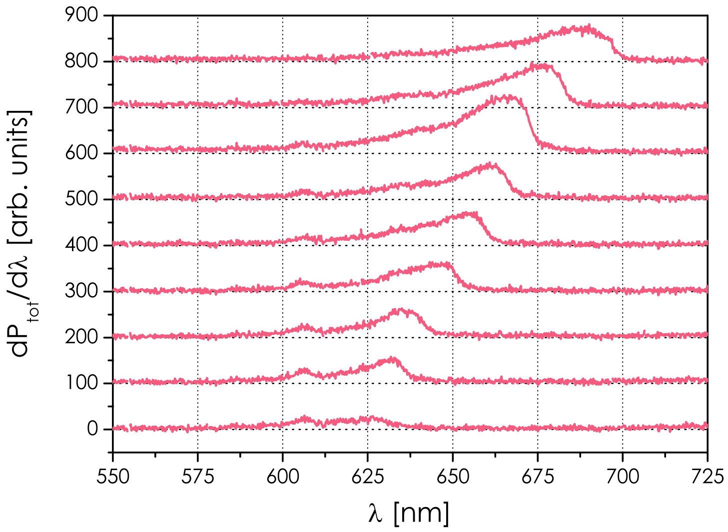

Figure 8. Emission spectra of a single NV^- center for different values of the air gap d_0 between the LR and HR mirrors. From the bottom of the graph to the top, the cavity length is increased using piezoelectric actuators. We start from a configuration where the two mirrors are almost in contact, and pass through a distance between the mirror yielding a maximum intensity with a narrowing of the emission spectrum compared to free space emission. The small peak at 607 nm is the two-phonon Raman scattering line of the diamond nanocrystal matrix as observed in previous work [61], corresponding to a Raman shift of 1480 cm^{-1}, different from the one of 1335 cm^{-1} in the case of the bulk diamond crystal, probably due to the nanocrystalline form.

a transmission spectrum $\overline{T}(\lambda)$ averaged over the numerical aperture of O_2 and over the two polarizations TE and TM, as detailed in appendix A.

3.2. *Narrowing of the spectrum of a single* NV^- *color center coupled to one microcavity mode*

To identify well-isolated fluorescent emitters, we first raster scan the sample. For each fluorescent spot, the uniqueness of the emitter is then checked by the observation of antibunching in the photon statistics of the fluorescent light. Since after the emission of a first photon it takes a finite time for a single emitter to be excited again and then it spontaneously emits a second photon, the antibunching effect appears as a dip around zero delay $\tau = 0$ in the normalized intensity $I(t)$ time autocorrelation function,

$$g^{(2)}(\tau) \equiv \frac{\langle I(t)I(t+\tau)\rangle}{\langle I(t)\rangle^2}. \qquad (6)$$

The HBT detection setup allows one to record the histogram of time delays between two consecutively detected photons on each avalanche photodiode (APD). Considering our detection efficiency of a few per cent, this histogram is a very good approximation of the intensity autocorrelation function $g^{(2)}(\tau)$.

Figure 8 shows different emission spectra measured for the same single NV center with changing cavity length. The first spectrum at the bottom is obtained for a closed cavity

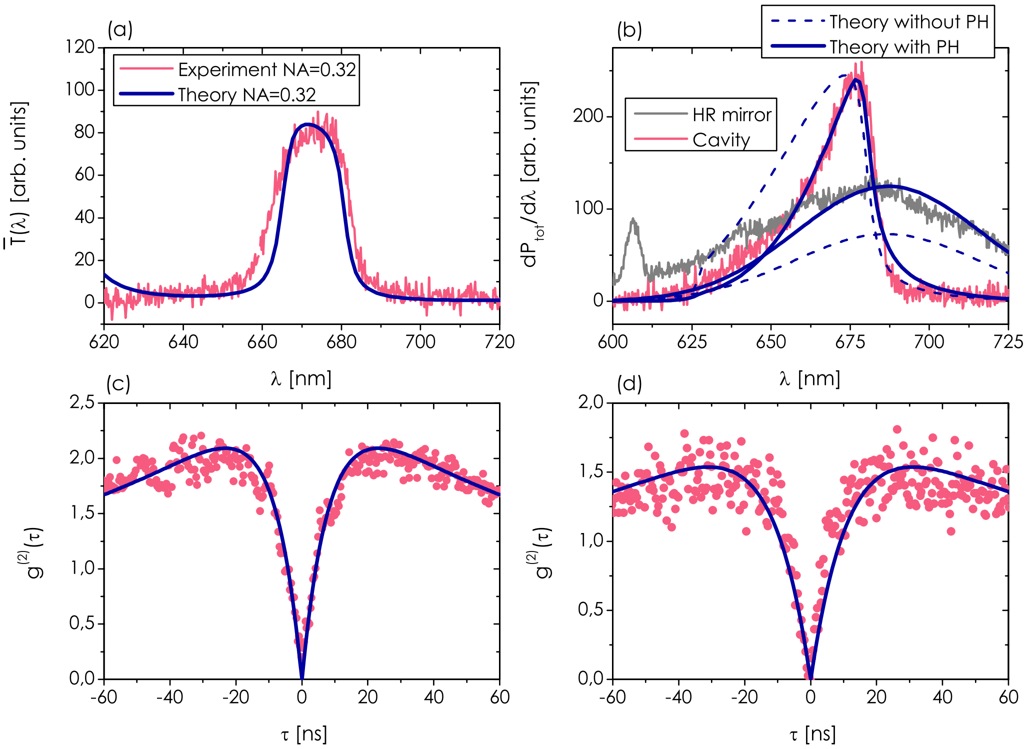

Figure 9. (a) Transmission spectrum of the microcavity obtained with its illumination by a white light source at NA = 0.32 (see figure 7). We also show a calculated transmission spectrum obtained for $d_0 = 124.1$ nm. (b) Emission spectra of single NV centers on an HR mirror (gray plot) or inside a cavity (pink plot). The calculations are normalized using the microcavity spectrum. We give two sets of calculated spectra: (i) dash curve: without taking into account the pinhole (PH) spatial filtering; and (ii) full line: taking into account the confocal PH filtering and a negative defocusing. The small peak around 607 nm of graph (b) is a Raman scattering line of the diamond matrix. Time–intensity correlation function $g^{(2)}$ displaying photon antibunching in two cases: (c) a single NV center on an HR mirror and (d) a single NV center inside the microcavity. The fits (blue lines) of the correlation functions have been carried out using the model given in [62].

(i.e. HR and LR mirrors in optical contact). In this configuration, there is no resonant mode in the Bragg mirror stop band and the fluorescence of the center is inhibited.

By opening the cavity, we increase the resonant wavelength corresponding to $m_c = 3$ and we obtain a resonant mode whose wavelength is located inside the emission spectrum of the NV^- center. We observe that the emitted fluorescence intensity is maximal with a noticeable shrinking of the spectrum when the resonant wavelength λ_0 is slightly detuned from the free space NV^- center emission maximum λ_{NV}^{max} (see the third curve starting from the top of figure 8).

Figure 9(a) shows a detailed analysis of one of the optimal configurations. The averaged experimental transmission $\overline{T}(\lambda)$ has been measured and this optimal case corresponds to the situation where the cavity resonant wavelength is almost tuned at the emission maximum.

Here, the optimal detuning δ is almost zero since the experimental value of NA is only 0.6. Figure 9(b) displays the cavity emission spectrum and the HR mirror emission spectrum (used as reference) recorded in the same experimental conditions. In particular, the saturation of the single NV center has been reached for the two configurations. Finally, figures 9(c) and (d) are time–intensity second-order correlation functions $g^{(2)}$ associated with the emission of a single NV center, for the mirror and cavity configurations, respectively. The vanishing dip at zero delay $\tau = 0$ in the $g^{(2)}$ function ensures that we address a single color center in both the cases.

The fit of the transmission spectrum $\overline{T}(\lambda)$ of the cavity has been obtained using equation (A.1) and only adjusting the value of the air gap thickness (here $d_0 = 124.1$ nm and thus $\delta = 1.2$ nm) governing mainly the resonant wavelength value. As mentioned in appendix A, we consider that the numerical aperture value is limited by the illumination objective (NA = 0.32). The spectral width of the calculated linear transmission spectrum $\overline{T}(\lambda)$ is in good agreement with the experimental results. For the comparison between the experimental and theoretical fluorescence spectra, we had to take into account the characteristics of our confocal microscope. Indeed, it is not possible to reproduce the width and amplitude of the experimental spectra only using the expression of the overall radiated power $\mathrm{d}P_{\mathrm{tot}}/\mathrm{d}\lambda$ derived from equation (5). This is illustrated by the dashed theoretical curves of figure 9(b). We have normalized the theoretical calculations using the maximum of the microcavity spectrum. In this case, the theoretical HR mirror emission spectrum, normalized in the same way, does not fit the experimental data. The confocal aperture spatial filtering must be taken into account to obtain good agreement between the theory and the experimental results [63]. The model used to simulate the propagation across the microscope is described in appendix B. After fixing the value of d_0 obtained from the transmission spectrum fit, the defocusing δz (see appendix B) is the only adjustable experimental parameter. Note that we have already mentioned that we have experimentally selected the brightest emitters whose two orthogonal dipoles are parallel to the mirror plane. Consequently, we assume in the following calculations that $\Theta = \pi/2$ and $\alpha = 0$, as was the case in the theoretical part. The diameter of the confocal aperture $D = 50\,\mu$m is well adapted for the case of an emitter deposited on the HR mirror. In this case, the pinhole does not truncate the electric field distribution and we obtain an almost perfect collection efficiency for $\delta z = 0$. Calculations show that for an emitter inside the cavity, the pinhole diameter is not perfectly adapted. The collection efficiency is thus reduced with respect to the case of the HR mirror. This detrimental effect could be reduced by using a larger confocal aperture. The effect of the LR mirror on the imaging properties of the system is taken into account by using negative defocusing [64]. The theoretical calculations given in figure 9(b) have been performed using defocusing $\delta z = -1500$ nm almost corresponding to the optimal value for the overall signal collection. In this case, we obtain very good agreement simultaneously for the shape of the spectrum and for the relative amplitude between the reference (HR mirror) and the microcavity.

We show that the spectrum of a single NV center can be tailored using a planar microcavity in a similar way as for single molecules [41]. From a qualitative point of view, the fluorescence spectrum is asymmetric and shows profile steepening from its red side, which is in good agreement with other experimental observations in microcavity LEDs [65]. We also show good agreement between the experimental results and the theoretical calculations, taking into account the optical and geometrical properties of our experimental setup.

We then compared the performances of the sole HR mirror single-photon source with the one with the emitter inside the microcavity. Table 1 reports the total counting rates (sum of both APDs) and the counting rate spectral density for the two configurations at similar

Table 1. Counting rates of a single NV color center in the case of the two studied configurations: the HR mirror alone and the microcavity (HR + LR mirrors on the top). Note that the measurements were carried out on two different single emitters.

Configuration	Excitation laser power (mW)	Total photon counting rate (kcounts s^{-1})	Counting rate spectral density around λ_0 (counts s nm^{-1})
HR mirror	11.5	140	0.5
Microcavity	10.2	63	1.0

input excitation laser power. We measured 140 kcounts s^{-1} for the HR mirror configuration and 63 kcounts s^{-1} in the case of the microcavity. We thus observe a reduction of 55% between the HR mirror and the cavity case. The theory gives only a reduction of 27% due to the pinhole effect. The difference might come from the filtering of the parasitic light (e.g. Raman scattering) in the case of the cavity. Note that we would have obtained an increase to 70% without taking into account the pinhole filtering. However, we observed an interesting modification of the fluorescence in the cavity configuration: due to the narrowing of the emitted spectrum from $B \approx 75$ nm to $B \approx 22$ nm, the counting rate spectral density is twice as large in the microcavity case, which proves that the emission modes of the nanocrystal are to some extent coupled to some microcavity modes for which the fluorescence rate is enhanced.

4. Conclusion

We have shown theoretically using a simple dipole model embedded in a multilayer system that the fluorescence collection of a single NV diamond color center can be enhanced by a factor of two when it is placed into a moderate-finesse ($\mathcal{F} \approx 60$) microcavity with respect to its emission when it is located onto a single high-reflectivity mirror. The calculations were performed in practical configurations of either quantum information processing applications, taking advantage of the coherence of the photons emitted at the NV^- center zero phonon line under cryogenic temperature or of quantum key distribution corresponding to a room temperature operation and thus broadband emission of the NV center. In QIP applications using photons emitted in the ZPL [10], the microcavity could help us to enhance the ZPL fluorescence while reducing the emission in the phonon sidebands. In room temperature single-photon QKD, we could take advantage of the microcavity fluorescence spectrum narrowing to use moderate bandwidth optical elements. We also performed room temperature experiments using the NV color center in diamond nanocrystals and studied the effect of a planar microcavity on the detected fluorescence light from a single NV center. We have shown that the fluorescence spectrum can be narrowed using such a planar microcavity and that the counting rate spectral density can be increased compared to the use of a single HR mirror. Such a simultaneous spectrum narrowing and fluorescence spectral density enhancement brought by the microcavity represents a significant increase in the performances of the diamond NV color center-based single-photon source in the prospects of open-air QKD applications.

Acknowledgments

We thank Jean-Pierre Madrange for the realization of the microcavity mechanical parts and Thierry Gacoin for the preparation of the photoluminescent nanodiamonds sample. We acknowledge helpful discussions with Alexios Beveratos, Rosa Brouri-Tualle, Gaétan Messin and Jean-Philippe Poizat.

Appendix A. Linear transmission calculation in the case of a focused illumination

We give here the expression of the averaged transmission spectrum $\overline{T}(\lambda)$ of the microcavity used to reproduce the experimental results. We used the standard linear transmission $T(\lambda, \theta, P)$ calculated for a plane wave propagating in the θ direction with a polarization $P = \{\mathrm{TE}, \mathrm{TM}\}$ using the transfer matrix method [50] to evaluate the quantity

$$\overline{T}(\lambda) = \frac{1}{2(1-\cos\theta_M)} \int_0^{\theta_\mathrm{M}} [T(\lambda, \theta, \mathrm{TE}) + T(\lambda, \theta, \mathrm{TM})] \sin\theta \, \mathrm{d}\theta. \tag{A.1}$$

We assume that the beam limitation only comes from the numerical aperture of the microscope objective O_2 used to illuminate the microcavity with the white light, as shown in figure 7, and thus $\sin\theta_\mathrm{M} = 0.32$.

Appendix B. Theoretical description of the propagation in the imaging system

In this section, we give the method used to take into account the effect of the confocal aperture (diameter D) and the defocusing on the collection efficiency. The defocusing is taken into account by adding a perturbation to a reference wave surface propagating in our stigmatic optical system, as represented in figure B.1 [66, 67]. We consider here three wave surfaces: (i) Σ_f, which is the object focal sphere of radius f, (ii) a plane wave surface Σ located in the intermediary space between the microscope objective (focal f) and its tube lens of focal f' and (iii) the image focal sphere $\Sigma_{f'}$ of radius f'. We assume a perfect imaging system and these three surface waves are stigmatic. First we calculate the field $\mathbf{E}_f(\mathbf{q})$ (where we denote $\mathbf{q} = \mathbf{k}_+/k$) in the θ direction on the reference sphere Σ_f using equations (4). Then, we obtain the electric field on the plane wave surface Σ [68],

$$\mathbf{E}_\Sigma(\eta, \xi) = \frac{1}{\sqrt{\cos\theta}} \mathbf{E}_f(q_x = \eta/f, q_y = \xi/f, q_z), \tag{B.1}$$

where η and ξ are the coordinates of the intersection between the emerging ray and Σ. For a given direction characterized by θ' and the unitary vector $\mathbf{q}'$, we can write the emerging field on the surface $\Sigma_{f'}$,

$$\mathbf{E}_{f'}(\mathbf{q}') = \sqrt{\cos\theta'} \cdot \mathbf{E}_\Sigma(\eta = q'_x f', \xi = q'_y f') \mathrm{e}^{\mathrm{j}\varphi_\mathrm{def}(\theta')}. \tag{B.2}$$

The additional phase term φ_def accounts for the image space defocusing $\delta z'$,

$$\varphi_\mathrm{def}(\theta') = -\frac{2\pi\delta z'}{\lambda}(1-\cos\theta'). \tag{B.3}$$

For a given object aperture angle θ, the corresponding image angle θ' is calculated using $\rho = f\sin\theta = f'\sin\theta'$, where $\rho = \sqrt{\eta^2 + \xi^2}$ [68]. The defocusing value in the image space $\delta z'$ is connected to the defocusing in the object space δz using the sine and Herschel conditions

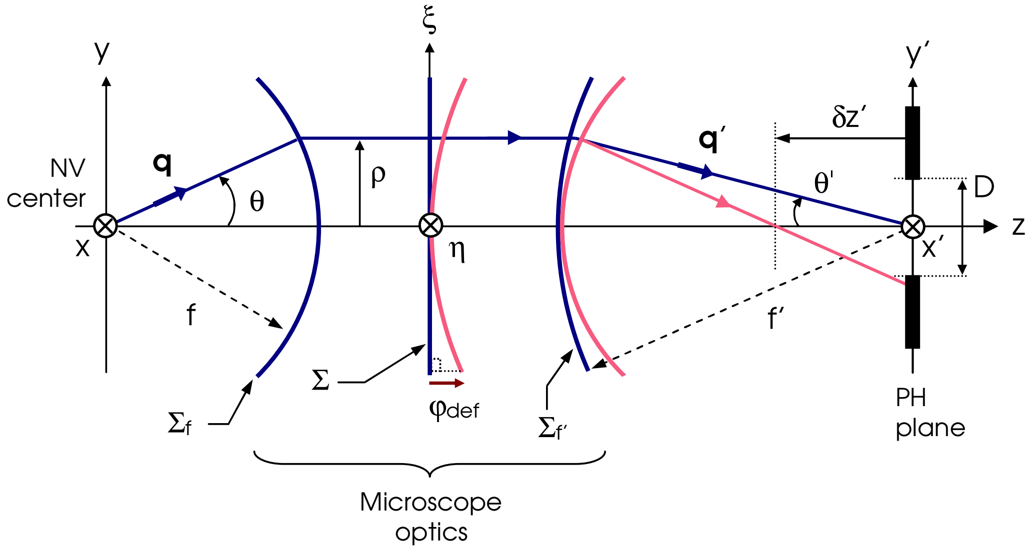

Figure B.1. The reference focal sphere Σ_f is centered on the emitter. This surface is transformed into a plane Σ between the objective and the tube lens. In the presence of defocusing $\delta z'$, the reference sphere is changed by adding a phase term φ_{def}. The confocal aperture (PH) of diameter D is located at the center of the unperturbed reference focal sphere $\Sigma_{f'}$. Both the refractive indices of the object and image spaces are equal to 1.

denoting that $f'/f = G_t$, where $G_t = 40$ is the magnification of the objective O_1. In the image space, the numerical aperture is weak and the paraxial approximation can be used. In particular, the electric field $\mathbf{E}$ in the focal plane (x', y') can be calculated using a Fourier transform (FT),

$$\mathbf{E}_{\mathrm{PH}}(x'/\lambda, y'/\lambda) = \mathrm{FT}[\mathbf{E}_{f'}(\eta/f', \xi/f')]. \tag{B.4}$$

We can thus obtain the intensity distribution in the image plane by keeping only the x'- and y'-components of $\mathbf{E}_{\mathrm{PH}}$ [64, 66], which allows the collected spectral density power to be calculated by an integration over the pinhole area,

$$\frac{\mathrm{d}P_{\mathrm{tot}}}{\mathrm{d}\lambda}(\lambda) = \frac{c\epsilon_0}{2}\iint_{\mathrm{PH}} f(\lambda)[|E_{\mathrm{PH},x'}(x'/\lambda, y'/\lambda)|^2 + |E_{\mathrm{PH},y'}(x'/\lambda, y'/\lambda)|^2]\mathrm{d}x'\,\mathrm{d}y'. \tag{B.5}$$

This last equation has been used to obtain the fit in the plain line shown in figure 9(b).

References

[1] Ladd T D, Jelezko F, Laflamme R, Nakamura Y, Monroe C and O'Brien J L 2010 Quantum computers *Nature* **464** 45–53

[2] Kurtsiefer C, Mayer S, Zarda P and Weinfurter H 2000 Stable solid-state source of single photons *Phys. Rev. Lett.* **85** 290–3

[3] Beveratos A, Brouri R, Gacoin T, Villing A, Poizat J-P and Grangier P 2002 Single photon quantum cryptography *Phys. Rev. Lett.* **89** 187901

[4] Alléaume R, Treussart F, Messin G, Dumeige Y, Roch J-F, Beveratos A, Brouri-Tualle R, Poizat J-P and Grangier P 2004 Experimental open-air quantum key distribution with a single-photon source *New J. Phys.* **6** 92

[5] Jacques V, Wu E, Grosshans F, Treussart F, Grangier P, Aspect A and Roch J-F 2007 Experimental realization of Wheeler's delayed-choice gedanken experiment *Science* **315** 966–8

[6] Kennedy T A, Colton J S, Butler J E, Linares R C and Doering P J 2003 Long coherence times at 300 K for nitrogen-vacancy center spins in diamond grown by chemical vapor deposition *Appl. Phys. Lett.* **83** 4190–2

[7] Jelezko F, Gaebel G, Popa I, Domhan M, Gruber A and Wrachtrup J 2004 Observation of coherent oscillation of a single nuclear spin and realization of a two-qubit conditional quantum gate *Phys. Rev. Lett.* **93** 130501

[8] Childress L, Gurudev Dutt M V, Taylor J M, Zibrov A S, Jelezko F, Wrachtrup J, Hemmer P R and Lukin M D 2006 Coherent dynamics of coupled electron and nuclear spin qubits in diamond *Science* **314** 281–5

[9] Jelezko F, Gaebel T, Popa I, Gruber A and Wrachtrup J 2004 Observation of coherent oscillations in a single electron spin *Phys. Rev. Lett.* **92** 076401

[10] Togan E *et al* 2010 Quantum entanglement between an optical photon and a solid-state spin qubit *Nature* **466** 730–4

[11] Balasubramanian G *et al* 2008 Nanoscale imaging magnetometry with diamond spins under ambient conditions *Nature* **455** 648–52

[12] Maze J R *et al* 2008 Nanoscale magnetic sensing with an individual electronic spin in diamond *Nature* **455** 644–7

[13] Moreau E, Robert I, Gérard J-M, Abram I, Manin L and Thierry-Mieg V 2001 Single-mode solid-state single photon source based on isolated quantum dots in pillar microcavities *Appl. Phys. Lett.* **79** 2865–7

[14] Barnes W L, Björk G, Gérard J-M, Jonsson P, Wasey J A E, Worthing P T and Zwiller V 2002 Solid-state single photon sources: light collection strategies *Eur. Phys. J.* D **18** 197–210

[15] Tomljenovic-Hanic S, Steel M J, de Sterke C M and Salzman J 2006 Diamond based photonic crystal microcavities *Opt. Express* **14** 3556–62

[16] Kreuzer C, Riedrich-Möller J, Neu E and Becher C 2008 Design of photonic crystal microcavities in diamond films *Opt. Express* **16** 1632–44

[17] Tomljenovic-Hanic S, Greentree A D, de Sterke C M and Prawer S 2009 Flexible design of ultrahigh-Q microcavities in diamond-based photonic crystal slabs *Opt. Express* **17** 6465–75

[18] Wang C F, Hanson R, Awschalom D D, Hu E L, Feygelson T, Yang J and Butler J E 2007 Fabrication and characterization of two-dimensional photonic crystal microcavities in nanocrystalline diamond *Appl. Phys. Lett.* **91** 201112

[19] Wang C F, Choi Y-S, Lee J C, Hu E L, Yang J and Butler J E 2007 Observation of whispering gallery modes in nanocrystalline diamond microdisks *Appl. Phys. Lett.* **90** 081110

[20] Park Y-S, Cook A K and Wang H 2006 Cavity QED with diamond nanocrystals and silica microspheres *Nano Lett.* **6** 2075–9

[21] Fu K-M, Santori C, Spillane S M, Fattal D, Xu Q, Fiorentino M, Beausoleil R G, Barclay P E and Painter O 2008 Coupling single NV centers in diamond to optical microcavities *Conf. on Lasers and Electro-Optics/Quantum Electronics and Laser Science Conference and Photonic Applications Systems Technologies, OSA Technical Digest* paper JMB3 1–2

[22] Schietinger S, Schröder T and Benson O 2009 One-by-one coupling of single defect centers in nanodiamonds to high-Q modes of an optical microresonator *Nano Lett.* **8** 3911–5

[23] Schietinger S and Benson O 2009 Coupling single NV-centres to high-Q whispering gallery modes of a preselected frequency-matched microresonator *J. Phys. B: At. Mol. Opt. Phys.* **42** 114001

[24] Gregor M, Henze R, Schröder T and Benson O 2009 On-demand positioning of a preselected quantum emitter on a fiber-coupled toroidal microresonator *Appl. Phys. Lett.* **95** 153110

[25] Barclay P E, Fu K-M, Santori C and Beausoleil R G 2009 Chip-based microcavities coupled to nitrogen-vacancy centers in single crystal diamond *Appl. Phys. Lett.* **95** 191115

[26] Zhang Y and Lončar M 2009 Submicrometer diameter micropillar cavities with high quality factor and ultrasmall mode volume *Opt. Lett.* **34** 902–4

[27] McCutcheon M W and Lončar M 2008 Design of a silicon nitride photonic crystal nanocavity with a quality factor of one million for coupling to a diamond nanocrystal *Opt. Express* **16** 19136–45

[28] Barclay P E, Fu K M, Santori C and Beausoleil R G 2009 Hybrid photonic crystal cavity and waveguide for coupling to diamond NV-centers *Opt. Express* **17** 9588–601

[29] Barth M, Nüsse N, Löchel B and Benson O 2009 Controlled coupling of a single-diamond nanocrystal to a photonic crystal cavity *Opt. Lett.* **34** 1108–10

[30] Wolters J, Schell A W, Kewes G, Nüsse N, Schoengen M, Döscher H, Hannappel T, Löchel B, Barth M and Benson O 2010 Enhancement of the zero phonon line emission from a single nitrogen vacancy center in a nanodiamond via coupling to a photonic crystal cavity *Appl. Phys. Lett.* **97** 141108

[31] Englund D, Shields B, Rivoire K, Hatami F, Vučković J, Park H and Lukin M D 2010 Deterministic coupling of a single nitrogen vacancy center to a photonic crystal cavity *Nano Lett.* **10** 3922–6

[32] Stewart L A, Zhai Y, Dawes J M, Steel M J, Rabeau J R and Withford M J 2009 Single photon emission from diamond nanocrystals in an opal photonic crystal *Opt. Express* **17** 18044–53

[33] Babinec T M, Hausmann B J M, Khan M, Zhang Y, Maze J R, Hemmer P R and Lončar M 2010 A diamond nanowire single-photon source *Nat. Nanotechnol.* **5** 195–9

[34] Purcell E M 1946 Spontaneous emission probabilities at radio frequencies *Phys. Rev.* **69** 681

[35] Su C-H, Greentree A D and Hollenberg L C L 2008 Towards a picosecond transform-limited nitrogen-vacancy based single photon source *Opt. Express* **16** 6240–50

[36] Drexhage K H 1970 Influence of a dielectric interface on fluorescence decay time *J. Lumin.* **1–2** 693–701

[37] Lukosz W 1979 Light emission by magnetic and electric dipoles close to a plane dielectric interface. III. Radiation patterns of dipoles with arbitrary orientation *J. Opt. Soc. Am.* **69** 1495–503

[38] Enderlein J 2002 Spectral properties of a fluorescing molecule within a spherical metallic nanocavity *Phys. Chem. Chem. Phys.* **4** 2780–6

[39] Steiner M, Schleifenbaum F, Stupperich C, Failla A V, Hartschuh A and Meixner A J 2005 Microcavity-controlled single-molecule fluorescence *ChemPhysChem* **6** 2190–6

[40] Steiner M, Failla A V, Hartschuh A, Schleifenbaum F, Stupperich C and Meixner A J 2008 Controlling molecular broadband-emission by optical confinement *New J. Phys.* **10** 123017

[41] Chizhik A, Schleifenbaum F, Gutbrod R, Chizhik A, Khoptyar D, Meixner A J and Enderlein J 2009 Tuning the fluorescence emission spectra of a single molecule with a variable optical subwavelength metal microcavity *Phys. Rev. Lett.* **103** 073002

[42] Qualtieri A *et al* 2009 Nonclassical emission from single colloidal nanocrystals in a microcavity: a route towards room temperature single photon sources *New J. Phys.* **11** 033025

[43] Kitson S C, Jonsson P, Rarity J G and Tapster P R 1998 Intensity fluctuation spectroscopy of small numbers of dye molecules in microcavity *Phys. Rev.* A **58** 620–7

[44] Benisty H, De Neve H and Weisbuch C 1998 Impact of planar microcavity effects on light extraction – Part I: basic concepts and analytical trends *J. Quantum Electron.* **34** 1612–31

[45] Benisty H, De Neve H and Weisbuch C 1998 Impact of planar microcavity effects on light extraction. Part II: selected exact simulations and role of photon recycling *J. Quantum Electron.* **34** 1632–43

[46] Beveratos A, Brouri R, Gacoin T, Poizat J-P and Grangier P 2001 Nonclassical radiation from diamond nanocrystals *Phys. Rev.* A **64** 061802

[47] Begon C, Rigneault H, Jonsson P and Rarity J G 2000 Spontaneous emission control with planar dielectric structures: an asset for ultrasensitive fluorescence analysis *Single Mol.* **1** 207–14

[48] Rigneault H and Monneret S 1996 Modal analysis of spontaneous emission in a planar microcavity *Phys. Rev.* A **54** 2356–8

[49] Beveratos A, Kühn S, Brouri R, Gacoin T, Poizat J-P and Grangier P 2002 Room temperature stable single-photon source *Eur. Phys. J.* D **18** 191–6

[50] Yeh P, Yariv A and Hong C 1977 Electromagnetic propagation in periodic stratified media. I. General theory *J. Opt. Soc. Am.* **67** 423–38

[51] Davies G and Hamer M F 1976 Optical studies of the 1.945 eV vibronic band *Proc. R. Soc.* A **348** 285–98

[52] Epstein R, Mendoza F M, Kato Y K and Awschalom D D 2005 Anisotropic interactions of a single spin and dark-spin spectroscopy in diamond *Nat. Phys.* **1** 94–8

[53] Mayer Alegre T P, Santori C, Medeiros-Ribeiro G and Beausoleil R G 2007 Polarization-selective excitation of nitrogen vacancy centers in diamond *Phys. Rev.* B **76** 165205

[54] Benisty H, Stanley R and Mayer M 1998 Method of source for dipole emission modification in modes of arbitrary planar structures *J. Opt. Soc. Am.* A **15** 1192–201

[55] Enderlein J, Ruckstuhl T and Seeger S 1999 Highly efficient optical detection of surface-generated fluorescence *Appl. Opt.* **38** 724–32

[56] Dräbenstedt A, Fleury L, Tietz C, Jelezko F, Kilin S, Nizovtzev A and Wrachtrup J 1999 Low-temperature microscopy and spectroscopy on single defect centers in diamond *Phys. Rev.* B **60** 11503–8

[57] Beveratos A 2002 Réalisation expérimentale d'une source de photons uniques par fluorescence de centres colorés dans le diamant; application à la cryptographie quantique *PhD Thesis* Université Paris-Sud 11, Orsay, France (http://tel.archives-ouvertes.fr/tel-00008487/en/)

[58] Oulton R F, Stavrinou P N and Parry G 2005 Optical coherence of planar microcavity emission *Appl. Phys.* B **80** 817–21

[59] Kurtsiefer C, Zarda P, Mayer S and Weinfurter H 2001 The breakdown flash of silicon avalanche photodiodes—back door for eavesdropper attacks? *J. Mod. Opt.* **48** 2039–47

[60] Treussart F, Clouqueur A, Grossman C and Roch J-F 2001 Photon antibunching in the fluorescence of a single dye molecule embedded in a thin polymer film *Opt. Lett.* **26** 1504–6

[61] Dumeige Y, Treussart F, Alléaume R, Gacoin T, Roch J-F and Grangier P 2004 Photo-induced creation of nitrogen-related color centers in diamond nanocrystals under femtosecond illumination *J. Lumin.* **109** 61–7

[62] Beveratos A, Brouri R, Poizat J-P and Grangier P 2001 Bunching and antibunching from single NV color centers in diamond *Proc. Quantum Communication, Computing and Measurement 3* ed P Tombesi and O Hirota (Dordrecht: Kluwer) 261–7

[63] Enderlein J 2000 Theoretical study of detection of a dipole emitter through an objective with high numerical aperture *Opt. Lett.* **25** 634–6

[64] Haeberlé O, Ammar M, Furukawa H, Tenjimbayashi K and Török P 2003 Point spread function of optical microscopes imaging through stratified media *Opt. Express* **11** 2964–9

[65] Oulton R F, Gray J W, Stavrinou P N and Parry G 2001 Insight into planar microcavity emission as a function of numerical aperture *Opt. Commun.* **195** 327–38

[66] Born M and Wolf E 1980 *Principles of Optics: Electromagnetic Theory of Propagation, Interference and Diffraction of Light* 6th edn (Oxford: Pergamon)

[67] Brokmann X 2004 Propriétés de fluorescence de nanocristaux de CdSe individuels *PhD Thesis* Université Paris VI, Paris, France (http://tel.archives-ouvertes.fr/tel-00007873/fr/)

[68] Richards B and Wolf E 1959 Electromagnetic diffraction in optical systems. II. Structure of the image field in an aplanetic system *Proc. R. Soc.* A **253** 358–79